

# Gyroidal Porous Carbon Activated with NH<sub>3</sub> or CO<sub>2</sub> as Lithium–Sulfur Battery Cathodes

Benjamin Krüner,<sup>[a, b]</sup> Tobias S. Dörr,<sup>[a, b]</sup> Hwirim Shim,<sup>[a, b]</sup> Joachim Sann,<sup>[c]</sup> Jürgen Janek,<sup>[c]</sup> and Volker Presser<sup>\*[a, b]</sup>

Ordered mesoporous carbon materials, prepared from co-assembly of a block copolymer and a commercial resol, were investigated as a sulfur host for LiS-battery cathodes. We studied two activation methods for such carbons, namely annealing in ammonia (NH<sub>3</sub>) and carbon dioxide (CO<sub>2</sub>). We found that both activation environments drastically increased the specific surface area and establish a micro- and mesoporous pore structure. Treatment with NH<sub>3</sub> also introduced nitrogen

groups, which increased the initial specific capacity. The non-activated carbon yielded carbon/sulfur cathodes with an initial capacity of ~900 mAh/g<sub>sulfur</sub> (150 mAh/g<sub>sulfur</sub> after 100 cycles). The initial capacity was increased to 1300 mAh/g<sub>sulfur</sub> for the NH<sub>3</sub> activated sample but with poor cycling stability. Enhanced performance stability was found for the CO<sub>2</sub> treated sample with an initial capacity of 1100 mAh/g<sub>sulfur</sub> (700 mAh/g<sub>sulfur</sub> after 100 cycles).

## 1. Introduction

Lithium-sulfur batteries (LiS) with their high theoretic specific capacity of 1672 mAh/g<sub>sulfur</sub> are promising for advanced energy storage considering that sulfur is an abundant, cheap, and low-toxic resource.<sup>[1–4]</sup> Sulfur itself shows a very low electrical conductivity; LiS cathodes, therefore, require hybridization of sulfur with a conductive matrix material, such as carbon.<sup>[2,4]</sup> Various microporous,<sup>[5,6]</sup> mesoporous,<sup>[7–10]</sup> and hierarchical porous carbon composites<sup>[11–13]</sup> have been reported as highly conductive matrices to encapsulate the sulfur. An advanced pore structure can increase the performance of LiS-batteries and reduce the sulfur shuttling, which is one of the main reasons for the LiS-battery degradation.<sup>[14]</sup> Especially microporous and hierarchical porous carbons reduce polysulfide shuttling due to the confinement of the polysulfides to nanopores.<sup>[2,11–13,15,16]</sup> There are many different synthesis methods to produce advanced pore structures, like soft-templating, hard-templating, in-situ-templating, or using biomass precursors.<sup>[14]</sup> The material properties and pore structures will depend on the choice of synthesis method and the set of employed process parameters.

In 2015, Werner et al.<sup>[17]</sup> and Choudhury et al.<sup>[18]</sup> synthesized ordered gyroidal mesoporous carbons for LiS-batteries with

promising performance owed to the homogeneous winding pore structure. Werner et al. used a triblock terpolymer poly(isoprene)-block-poly(styrene)-block-poly(ethylene oxide) (ISO) and either phenol-formaldehyde resin or oligomeric resorcinol-formaldehyde to produce different gyroidal mesoporous structures by co-assembly, followed by carbonization in argon at 900–1600 °C.<sup>[17,19]</sup> An additional removal of a template to produce the ordered mesopores is unnecessary, because the ISO decomposes at high temperatures. They also carried out physical activation of carbon with CO<sub>2</sub> to create suitable micropores that encapsulate the sulfur. This hierarchical activated carbon was used to produce a carbon/sulfur (ratio 1:1) hybrid electrode with a specific capacity of 830 mAh/g<sub>sulfur</sub> after 100 cycles.<sup>[17]</sup> Choudhury et al. produced gyroidal carbon by co-assembly of poly(styrene)-block-poly(4-vinylpyridine) block copolymer (PS-b-P4VP) with 3-pentadecylphenol (PDP).<sup>[18]</sup> They selectively removed the PDP with ethanol and backfilled the structure by a resorcinol-formaldehyde solution which was cross-linked and carbonized at 900 °C. The carbon was melt-infiltrated with sulfur in a ratio of 1:2. The initial specific capacity of the LiS-battery was around 600 mAh/g<sub>sulfur</sub> and decreased to ~450 mAh/g<sub>sulfur</sub> after 100 cycles measured at low C-rates (i.e., 0.2C for charging and 0.1 for discharging) in a potential window of 1.8–2.6 V.

Next to an ordered pore structure, also nitrogen groups are reported to reduce sulfur shuttling because of strong N–S bonding.<sup>[16,20–24]</sup> Nitrogen can also enhance the activity towards sulfur reduction and, thereby, provides a higher initial capacity.<sup>[23,25,26]</sup> The many methods to produce nitrogen-doped porous carbon mainly follow two approaches:<sup>[27]</sup> either direct pyrolysis of nitrogen-containing precursors (e.g., melamine resin,<sup>[28–31]</sup> polypyrrole,<sup>[32]</sup> or biomass<sup>[33]</sup>) or post-synthesis treatment of carbon with nitrogen-containing compounds (e.g., NH<sub>3</sub>,<sup>[34]</sup> HCN,<sup>[35]</sup> or HNO<sub>3</sub><sup>[36,37]</sup>). One disadvantage of the direct use of nitrogen-containing precursors is that the functional groups may be released at high pyrolysis temperatures.<sup>[30]</sup> In

[a] B. Krüner, T. S. Dörr, H. Shim, Prof. V. Presser  
INM-Leibniz Institute for New Materials, 66123 Saarbrücken, Germany  
E-mail: volker.presser@leibniz-inm.de

[b] B. Krüner, T. S. Dörr, H. Shim, Prof. V. Presser  
Department of Materials Science and Engineering, Saarland University,  
66123 Saarbrücken, Germany

[c] Dr. J. Sann, Prof. Dr. J. Janek  
Institute of Physical Chemistry & Center for Materials Research, Justus-Liebig  
University Giessen,  
35392 Giessen, Germany

Supporting Information and the ORCID identification number(s) for the author(s) of this article can be found under:  
<https://doi.org/10.1002/batt.201800013>

contrast, post-synthesis treatments are an elegant way to modify a given material without changing the initial reaction parameters. However, this approach might form additional functional surface groups instead of actual nitrogen doping.<sup>[27,34,37]</sup> Wang et al. combined block copolymer co-assembly using a commercial Pluronic F127 and an in-situ doping during pyrolysis in ammoniacal atmosphere.<sup>[38]</sup> They obtained a mesoporous carbon containing up to 9 at% nitrogen in the form of pyridine, pyrrole, pyridone, and quaternary nitrogen groups after the treatment at 850 °C.<sup>[38]</sup> The resulting material showed a BET surface area of around 1400 m<sup>2</sup>/g with an average pore diameter of 7 nm and was used as an electrode for supercapacitors. We applied the in-situ doping during pyrolysis in NH<sub>3</sub> to sub-micrometer sized novolac beads in a previous study.<sup>[39]</sup> Thereby, it was possible to achieve micro-porous carbon beads with a nitrogen content of 5–7 mass% depending on the target temperature (750–950 °C).

In this study, we combine the beneficial pore size of a mesoporous carbon prepared by co-assembly of an optimized ISO block copolymer with in-situ activation upon pyrolysis. We synthesized three different samples: a mainly mesoporous carbon (pyrolyzed in argon), hierachic (meso- and micro-porous) carbon obtained after CO<sub>2</sub> activation, and a hierachic N-doped-carbon via activation in NH<sub>3</sub>. The homogeneous pore structure produced by the co-assembly makes this material attractive for fundamental investigations. The three carbons were used for carbon/sulfur hybrid LiS-battery cathodes to compare the influence of the two different activation methods on the electrochemical performance. Our work used a commercially available resol as the carbon source and a constant sulfur-to-carbon ratio of 2:1 considering industrial requirements.

## Experimental Section

### Materials

For the synthesis of ISO, benzene (99%, Alfa Aesar), *n*-butyllithium (nBuLi, 2.5 M in hexane, Alfa Aesar), 1,1-diphenylethylen (DPE, 98%, Alfa Aesar), isoprene (99%, <1000 ppm p-tert-butylcatechol, Sigma Aldrich), sec-butyllithium (secBuLi, 1.4 M in cyclohexane, Sigma Aldrich), styrene (ReagentPlus, stabilized, Sigma Aldrich), calcium hydride (CaH<sub>2</sub>, 1–20 mm granules, 88–98%, Alfa Aesar), ethylene oxide (EO, 99.8%, Praxair), potassium (98%, pieces in mineral oil, Fisher Scientific), naphthalene (99%, Fisher Scientific), tetrahydrofuran (THF, 99%, <1000 ppm Stabilizer, Alfa Aesar), chloroform (CHCl<sub>3</sub>, 99.8%, ACS, Alfa Aesar), methanol (MeOH, 99% AlfaAesar), hydrochloric acid (HCl, reagent grade, 37%, Sigma Aldrich), deuteriochloroform (CDCl<sub>3</sub>, 99.8 atom% D, Sigma Aldrich), and absolute tetrahydrofuran (THF<sub>abs</sub>, 99.85%, extra dry, non-stabilized, Acros Organics) were used as received, or purified as described below. The commercial phenolic resol (Phenodur PR 373) was obtained from Allnex. Elemental sulfur, polyvinylidene fluoride (PVDF) powder (molecular mass ca. 534.000 g/mol), *N*-methyl-2-pyrrolidone (NMP), bis(trifluoromethane)-sulfonimide lithium salt (LiTFSI), 1,2-dimethoxyethane (DME), 1,3-dioxolane (DOL), and lithium nitrate (LiNO<sub>3</sub>) were purchased from Sigma Aldrich. The battery-grade conductive carbon black (C65) was obtained from Imerys Graphite & Carbon and the nickel foil (thickness of 13 nm) from Carl Schlenk. Electrochemical grade high purity (99.9%) lithium was purchased from PI-KEM. Trilayer porous polyolefin

separator (type 2325) was obtained from Celgard, and we used non-woven polypropylene separators from Freudenberg.

### Synthesis

Poly(isoprene)-block-poly(styrene)-block-poly(ethylene oxide) (ISO) terpolymer was synthesized via living sequential anionic polymerization.<sup>[40,41]</sup> All chemicals were first purified by either nBuLi or CaH<sub>2</sub> and distilled under a reduced atmosphere. Sequential polymerization of the first two blocks was performed in benzene at room temperature using secBuLi as an initiator. The living poly(isoprene)-block-poly(styrene) was end-capped by ethylene oxide, deactivated by MeOH/HCl, and washed several times with MilliQ water. After drying in vacuum at 90 °C, the polymer was dissolved in THF and reactivated by potassium naphthalenide, and the last block was prepared. The final ISO was precipitated from CHCl<sub>3</sub> in an aliquot of MeOH, filtrated, and stored at 6 °C.

The ISO/resol hybrids were synthesized by a modified synthesis previously reported by Werner et al. (Ref. [19]). Briefly, a 4.0 mass% ISO in THF:CHCl<sub>3</sub> (1:1 by mass) stock solution was combined with 12.5 mass% resol (in THF) solution. The optimized structure was achieved with an ISO-to-resol mass ratio of 1:0.734 and a stirring time of 24 h. The mixture was then placed on a hotplate under a glass dome at 35 °C for 2 d for the evaporation-induced self-assembly (EISA). The resulting rubber-like hybrids were further aged successively from 90 °C to 130 °C to remove residual solvents and promote cross-linking.

The different activated mesoporous carbons were obtained by heating the ISO/resol hybrids in different atmospheres (Ar: G<sup>A</sup>-C-Ar, CO<sub>2</sub>: G<sup>A</sup>-C-CO<sub>2</sub> and NH<sub>3</sub>; G<sup>A</sup>-C-NH<sub>3</sub>) at 5 °C/min to 850 °C. The argon flow for all samples was constant with 50 cm<sup>3</sup>/min, and CO<sub>2</sub> or NH<sub>3</sub> was added to the inert gas. G<sup>A</sup>-C-Ar was held for 3 h at 850 °C only in Ar. The sample G<sup>A</sup>-C-CO<sub>2</sub> was heated in Ar and annealed for 3 h at a temperature of 850 °C with an additional CO<sub>2</sub> gas flow of 100 cm<sup>3</sup>/min. G<sup>A</sup>-C-NH<sub>3</sub> was also heated in a mixed Ar/NH<sub>3</sub> atmosphere with an NH<sub>3</sub> gas flow of 20 cm<sup>3</sup>/min while the argon flow was maintained at 50 cm<sup>3</sup>/min. This sample was held for 2.25 h at 850 °C in that specific gas mixture. Different annealing times for the heat treatment were necessary to achieve similar surface areas and allow the best comparability between the samples. The cooling was always carried out in an inert argon atmosphere. The carbon monoliths were ground in a mortar, and the particle size was reduced with a BeadBug Microtube homogenizer to a few micrometers.

Using melt infiltration, the carbon/sulfur hybrids were synthesized (G<sup>A</sup>-C-Ar/S, G<sup>A</sup>-C-CO<sub>2</sub>/S, and G<sup>A</sup>-C-NH<sub>3</sub>/S). The samples were homogenized in a mortar with sulfur and annealed at 155 °C for 5 h. Sulfur has its lowest viscosity at this temperature, and capillary forces assist the sulfur transport into the carbon pores.<sup>[7]</sup>

### Material Characterization

The synthesized ISO terpolymer was characterized by gel permeation chromatography (GPC) and <sup>1</sup>H nuclear magnetic resonance (NMR) spectroscopy. The molecular weight ( $M_w$ ) and polydispersity (PDI) of the terminated polyisoprene (PI) block (taken from the reaction during synthesis) was determined using a WATERS ambient-temperature GPC system equipped with a WATERS 2410 differential refractive index (RI) detector and a sample concentration of 1 mg/mL in THF. <sup>1</sup>H-NMR spectra after each polymerization step were recorded with a Bruker Advance III HD Nanobay equipped with a SampleXpress autosampler and a BBFO probe for 5 mm tubes. The samples were dissolved in CDCl<sub>3</sub> and measured at 300 MHz. The final  $M_w$  of the polymer was determined by normal-

ization of the PI  $^1\text{H-NMR}$  signal to the  $M_w$  determined by GPC. The overall polydispersity index (PDI) was further analyzed by GPC of the terminated terpolymer.

For small-angle X-ray scattering (SAXS) of the powdered sample after melt infiltration, an adequate piece of the polymer/resol hybrid or the monolithic carbon disc was sealed in polyimide tape. The measurements were performed on a Xenocs XEUS 2.0, equipped with a Dectris Pilatus 1 M detector (detector distance of 250 cm) and a Cu-K $\alpha$  source (154 pm). Calibration of the device was conducted with silver behenate, and total radial integration (with masking the primary beam) was performed for the 1D pattern.

We used for scanning electron microscopy (SEM) a JSM-7500F (Jeol) field emission scanning electron microscope with an operating voltage of 5 kV. Transmission electron microscopy (TEM) was carried out with a JEM-2100F (Jeol) and a high beam voltage of 200 kV. Energy dispersive X-ray spectroscopy (EDX) mapping was done at the TEM at 200 kV with an attached detector from Thermo Scientific (MC100021).

The porosity of the carbon materials was quantified by use of N<sub>2</sub> and CO<sub>2</sub> gas sorption analysis (Quantachrome Autosorb iQ). The samples were degassed at 300 °C for 20 h in a vacuum of 10 kPa to remove volatile components from the surface. The nitrogen measurements were performed in liquid nitrogen ( $-196^\circ\text{C}$ ) with a relative pressure between  $5 \cdot 10^{-7}$  and 1.0 in 76 steps. The CO<sub>2</sub> measurements were conducted at 0 °C with a relative pressure between  $7 \cdot 10^{-5}$  and 0.024 in 40 steps. A mixed quenched-solid density functional theory (QSDFT) assuming slit-like and cylindrical pores was applied to obtain the pore size distribution and specific surface area (SSA) above 0.9 nm from the N<sub>2</sub> isotherm and a non-local density functional theory (NLDFT) for deconvolution of the CO<sub>2</sub> isotherms for pore sizes below 0.9 nm.<sup>[42–44]</sup> We also used the Brunauer-Emmett-Teller (BET) equation in the linear part of the isotherm to obtain the SSA<sub>BET</sub>.<sup>[45]</sup> The calculations were carried out with the ASIQwin software.

X-ray photoelectron spectroscopy (XPS) measurements were conducted in a PHI Versaprobe II Scanning ESCA Microprobe (Physical Electronics) using a monochromatized Al-K $\alpha$  X-ray source (beam diameter 50 μm, X-ray power of 12.5 W). The analyzer pass energy for detail spectra was set to 11.75 eV with a step time of 50 ms and a step size of 0.1 eV. For the measurement, the sample was mounted on insulating tape and flooded with slow electrons and argon ions using the built-in ion sputter and electron guns to compensate the surface charge. Data evaluation was performed using CasaXPS software. The samples were already electronically conductive, were grounded during measurement with no further charge neutralization, and no further calibration was applied to the data. The analyzer itself was calibrated to a C1s C–C binding energy of 284.8 eV.

The chemical composition of the carbon/sulfur hybrids was determined with CHNS and O elemental analysis and thermogravimetric analysis (TGA). A vario MICRO cube system (Elementar Analysensysteme) oxidized the samples at 1150 °C in a tin sample holder, and the system was calibrated with sulfanilic acid (41.6 mass% C, 4.1 mass% H, 8.1 mass% N, 18.5 mass% S). The oxygen content was measured with a rapid OXY cube from Elementar at a pyrolysis temperature of 1450 °C. The device was calibrated with benzoic acid. The TGA measurements were performed with a Netzsch Libra TG 209 F1 in the temperature range from 25 °C to 700 °C with a heating rate of 10 °C/min under a constant flow of synthetic air.

Phase analysis was carried out with X-ray diffraction (XRD) and Raman spectroscopy. A D8 Advance diffractometer (Bruker AXS) with Cu-K $\alpha$  radiation (40 kV, 40 mA) was used in point focus mode

with a Goebel mirror and a 2D detector (Vantec-500). The samples were placed on a sapphire single crystal.

The Raman spectra were recorded with a Renishaw inVia system using laser power of 0.2 mW on the sample with an excitation wavelength of 632.8 nm, a grating of 1800 lines/mm, a recording time of 10 s per step, and 50 accumulations to reduce the signal to noise ratio. The D- and G-modes were fitted with four Voigt peaks.

## Electrochemical Measurements

The sulfur-infiltrated carbon samples were mixed with 10 mass% carbon black (C65) and 8 mass% PVdF (dissolved in NMP). The suspension was treated with a magnetic stirrer for 1 d and then coated on the nickel foil with a doctor blade (wet thickness: 200 μm). The electrodes were dried for ~16 h in the fume hood at room temperature and afterward heated to 80 °C in an oven for 8 h to evaporate any residual solvent. Then, electrode discs with a diameter of 14.2 mm were punched out and placed in a CR2032 coin cell in a two-electrode setup. A lithium disc with a diameter of 15.6 mm was used as a counter electrode with one Celgard 2325 separator. The amount of electrolyte is important for the performance of LiS-batteries.<sup>[46]</sup> Therefore, we used for the electrolyte (1 M LiTFSI + 0.25 M LiNO<sub>3</sub> in 1:1 DME/DOL by volume) a ratio to sulfur of 10.7 mL/g<sub>sulfur</sub>. The electrolyte was pipetted onto the electrode, and the Celgard 2325 separator was placed on it. The sealed coin cells were tested with a battery analyzer from Astrol (BatSmall) in galvanostatic charge/discharge mode at a constant current of 336 mA/g<sub>electrode</sub> (0.2C) for charging and 168 mA/g<sub>electrode</sub> (0.1C) for discharging in the potential window of 1.8 V to 2.6 V vs. Li/Li<sup>+</sup>. The charging rate was twice as large as the discharging rate. For rate capability measurements, the coin cells were measured at different rates from 0.1C (discharge)/0.2C (charge) for 20 cycles, 0.2C (discharge)/0.4C (charge) for the next 10 cycles, 0.5C (discharge)/1C (charge) for further 10 cycles, 1C (discharge)/2C (charge), and again 0.1C (discharge)/0.2C (charge) for the final 20 charging-discharging cycles. We normalized the capacity to the mass of sulfur or the mass of the electrodes, as seen from the labels "g<sub>sulfur</sub>" or "g<sub>electrode</sub>".

## 2. Results and Discussion

### 2.1. Material Characterization of the Three Gyroidal Materials

The simplified preparation of our different activated mesoporous carbon/sulfur hybrids is shown in Figure 1. The poly(isoprene)-block-poly(styrene)-block-poly(ethylene oxide) (ISO) comprises 31 vol%, 65 vol% and 4 vol% polyisoprene (PI), polystyrene (PS) and poly(ethylene oxide) (PEO), respectively, and has a PDI of  $D_p = 1.09$  at a total  $M_w$  of 51000 g/mol. In a first step, we selectively swelled the hydrophilic PEO by a commercial resol (see Supporting Information, Figures S1–S2). Through the evaporation-induced self-assembly (EISA) process, the mixture separated into phase-pure microdomains of each block. The resulting ISO/resol hybrid was pyrolyzed in different atmospheres to archive either mainly mesoporous carbon (argon; sample: G<sup>A</sup>-C-Ar) or hierarchically meso- and micro-porous carbon (CO<sub>2</sub>; sample: G<sup>A</sup>-C-CO<sub>2</sub>, and NH<sub>3</sub>; sample: G<sup>A</sup>-C-NH<sub>3</sub>). These carbons served as a conductive host material for the following melt-infiltration of sulfur.

Electron micrographs of the non-activated carbon (G<sup>A</sup>-C-Ar) are shown in Figure 2A–D. We did not observe noticeable

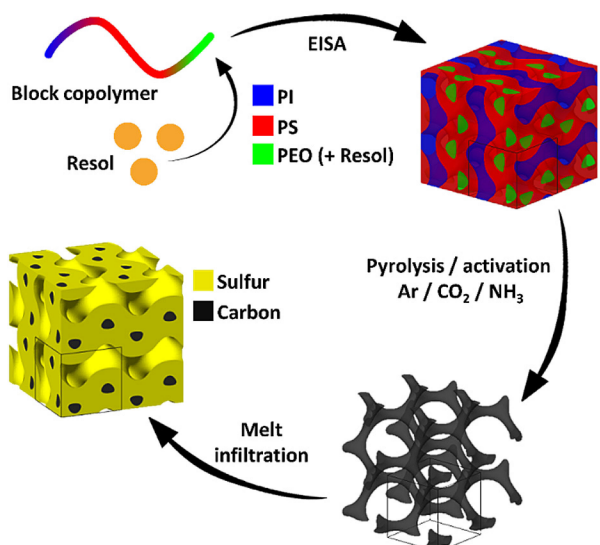


**Figure 1.** Schematic illustration of the synthesis of the gyroidal carbon/sulfur hybrid materials, by co-assembly, pyrolysis in Ar, CO<sub>2</sub>, or NH<sub>3</sub>, and melt infiltration with sulfur.

differences in the structure and morphology in the SEM images after the different activation conditions. By optimization of the preparation process and the ISO-to-resol ratio, we ensured a high degree of near- and long-range order of the resulting pore

system. Estimated from electron micrograph, we determined homogeneously distributed pores with an average pore size of 20 nm. The material shows no long-range ordering or highly crystalline structure, as can be seen from high-resolution TEM images (Figure 2D).

Results of the SAXS measurement of the ISO/resol hybrid and the various activated mesoporous carbon samples are provided in Figure 2E. From the first order diffraction ( $q^*$ ), we calculated the expected peak positions for allowed  $q/q^*$  ratios of the alternating gyroid ( $G^A$ ) morphology ( $q/q^* = 1, \sqrt{3}, \sqrt{4}, \sqrt{5}, \dots$ ) and give the fits above the corresponding pattern as triangles.<sup>[47]</sup> The ISO/resol hybrid with its low electron density difference of the components shows blurred peaks which are consistent with the  $G^A$  morphology and well preserved during pyrolysis in first and second order diffraction for the activated mesoporous carbons. From  $q^*$ , the periodicity ( $d_{100}$ ) was calculated to 50.4 nm for the ISO/resol hybrid, which shrinks during heat treatment by around 30% to 35.1 nm for  $G^A\text{-C-Ar}$ . The shift towards higher  $q^*$  values for the CO<sub>2</sub> and NH<sub>3</sub> activated carbons indicates a decreasing value for  $d_{100}$ . After activation, additional micropores blur the initially sharp interface boundaries (air/carbon), which results in peak broadening and no clear  $d_{100}$  peak can be identified.

We used nitrogen gas sorption at -196 °C and carbon dioxide gas sorption at 0 °C to characterize the porosity of our materials (Table 1). The nitrogen sorption isotherms of  $G^A\text{-C-CO}_2$

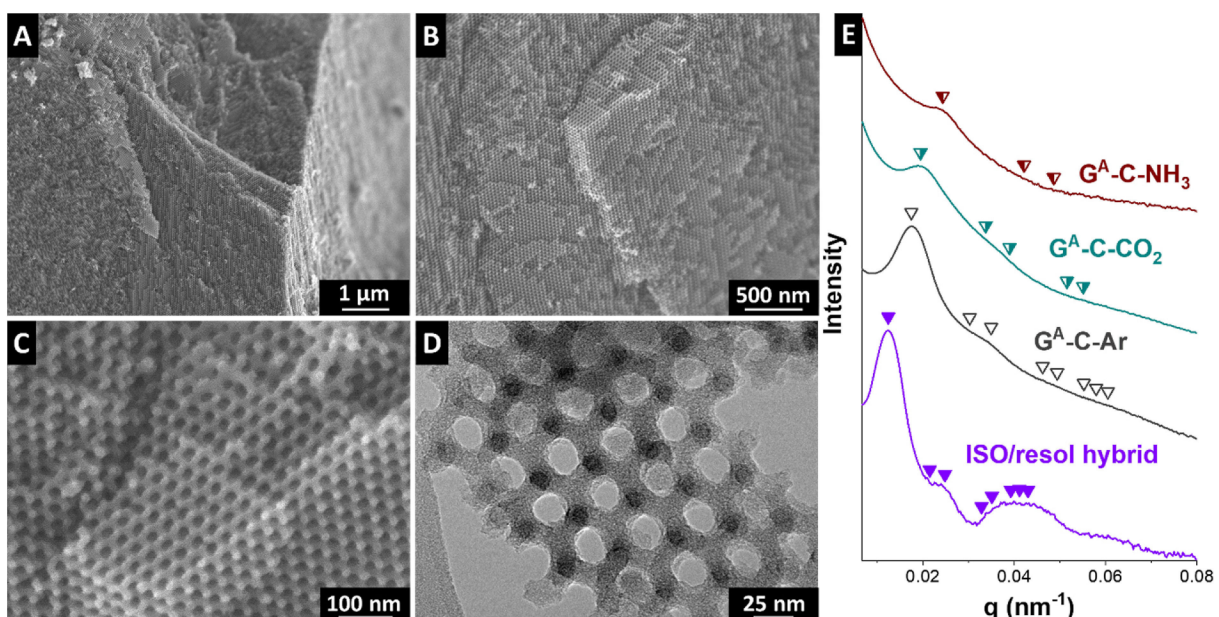


**Figure 2.** (A–C) SEM images of  $G^A\text{-C-Ar}$ . (D) TEM image of  $G^A\text{-C-Ar}$ . (E) SAXS pattern of the ISO/resol hybrid,  $G^A\text{-C-Ar}$ ,  $G^A\text{-C-CO}_2$ , and  $G^A\text{-C-NH}_3$ .

**Table 1.** Porosity data of the three samples obtained by the combination of CO<sub>2</sub> and N<sub>2</sub> gas sorption.

Sample	SSA <sub>BET</sub> [m <sup>2</sup> /g]	SSA <sub>DFT</sub> [m <sup>2</sup> /g]	Micropore volume [cm <sup>3</sup> /g]	Micropore volume [%]	Total pore volume [cm <sup>3</sup> /g]	Average micropore size [nm]	Average mesopore size [nm]
$G^A\text{-C-Ar}$	197	739	0.17	22	0.78	0.55	21.2
$G^A\text{-C-CO}_2$	1264	1530	0.43	33	1.29	0.62	22.7
$G^A\text{-C-NH}_3$	1191	1328	0.37	25	1.49	0.80	18.6

and  $G^A\text{-C-NH}_3$  are very similar and a mix of Type I(a) and Type II with Type H4 hysteresis loops, typical for micro-mesoporous carbons (Figure 3A).<sup>[48]</sup> In comparison, the sample  $G^A\text{-C-NH}_3$  shows lower adsorption in the low-pressure range and higher adsorption in the high-pressure range. This aligns with the calculated surface area of  $1264 \text{ m}^2/\text{g}$   $\text{SSA}_{\text{BET}}$  for  $G^A\text{-C-CO}_2$  and of  $1191 \text{ m}^2/\text{g}$   $\text{SSA}_{\text{BET}}$  for  $G^A\text{-C-NH}_3$ . The nitrogen sorption isotherm

of  $G^A\text{-C-Ar}$  shows a low nitrogen adsorption capacity in the low-pressure range, aligning with a low  $\text{SSA}_{\text{BET}}$  of  $197 \text{ m}^2/\text{g}$ . To investigate sub-nanometer pores more accurately, we also conducted  $\text{CO}_2$  sorption analysis (Figure 3B). As seen from these data, there is significant  $\text{CO}_2$  adsorption of  $G^A\text{-C-Ar}$  with an amplitude like  $G^A\text{-C-NH}_3$ . We used the NLDFT model assuming slit pores for deconvolution of the  $\text{CO}_2$  isotherms and calculated

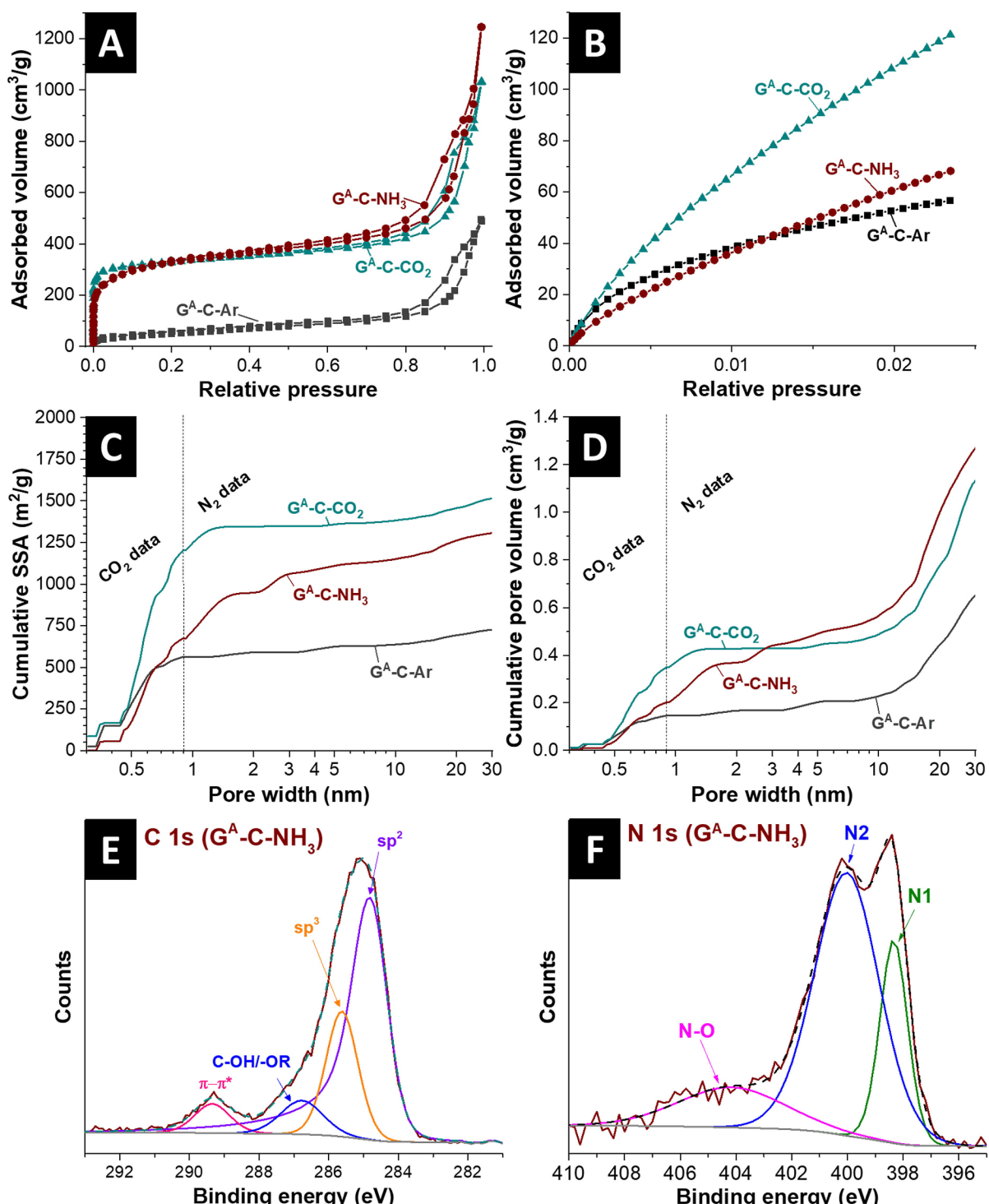


**Figure 3.** (A) Nitrogen and (B) carbon dioxide sorption isotherm with the combined pore size distribution of  $G^A\text{-C-Ar}$ ,  $G^A\text{-C-CO}_2$ , and  $G^A\text{-C-NH}_3$ . (C) Cumulative SSA and (D) cumulative pore volume calculated with density functional theory kernels. (E) C 1s and (F) N 1s signal of the XPS measurements sample  $G^A\text{-C-NH}_3$ .

the pore size distribution up to 0.9 nm for all samples. For larger pores, we used data from the  $N_2$  sorption isotherms and employed a QSDFT kernel. The resulting pore size distributions are shown in Figure 3C–D. The lowest  $SSA_{DFT}$  has  $G^A\text{-C-Ar}$  with  $739 \text{ m}^2/\text{g}$ , followed by  $G^A\text{-C-NH}_3$  with  $1328 \text{ m}^2/\text{g}$ , and  $G^A\text{-C-CO}_2$  with  $1530 \text{ m}^2/\text{g}$ .  $G^A\text{-C-Ar}$  also has the lowest pore volume of all materials with  $0.78 \text{ cm}^3/\text{g}$  and its average micropore size is 0.55 nm, while the mesopores have an average diameter of 21.2 nm. The micropore volume of  $G^A\text{-C-CO}_2$  is the highest with  $0.43 \text{ cm}^3/\text{g}$ , and the total pore volume is  $1.29 \text{ cm}^3/\text{g}$ . The micropores of  $G^A\text{-C-CO}_2$  are very small with an average value of 0.62 nm, while the mesopores are the largest in average with 22.7 nm. The activation with ammonia leads to a broader pore size distribution which results in a larger average micropore size of 0.80 nm and the largest total pore volume of all three materials with  $1.49 \text{ cm}^3/\text{g}$ .

The results of the elemental analysis (CHNOS) of the carbon materials are summarized in Table 2.  $G^A\text{-C-Ar}$  and  $G^A\text{-C-CO}_2$  have a very similar chemical composition: both mainly contain carbon (94 mass%) and oxygen (4 mass%), with negligible amounts of hydrogen and nitrogen. The  $\text{NH}_3$  activation introduced around 7 mass% nitrogen and increased the oxygen content to 9 mass%. The latter value is close to the composition of nitrogen-containing novolac-derived carbon beads which were produced under similar conditions in a previous study.<sup>[39]</sup>

We also quantified the chemical composition by XPS (Table 3). The high surface sensitivity of XPS indicates that the higher oxygen content of  $G^A\text{-C-CO}_2$  aligns with the larger amount of oxygen-containing functional groups at the activated surface.  $G^A\text{-C-NH}_3$  has a lower total amount of heteroatoms from XPS compared to the CHNS and O analyses, but a surplus of oxygen compared to nitrogen. The C 1s and N 1s spectra of  $G^A\text{-C-NH}_3$  are plotted in Figure 3E–F. Deconvolution of the N 1s signal allows the identification of nitrogen-containing groups.<sup>[49–51]</sup> We assign around 22% to pyridinic groups with its typical binding energy of 398 eV (N1).<sup>[50,51]</sup> 60% of nitrogen groups have a binding energy of 400 eV with a broadened signal, typical for pyrrolic, amine, and amide

groups.<sup>[51]</sup> Graphitic nitrogen groups have a binding energy of ~401 eV, and a minor fraction of these groups might be present as well.<sup>[50,51]</sup> A third kind of nitrogen group with a binding energy of 404 eV can be quantified with 18%, which relates to oxygen-bound nitrogen-like pyridine oxide.<sup>[51]</sup> The high amount of oxygen found in the chemical analysis aligns with this assumption. The absence of larger fractions graphitic nitrogen is in contrast to previous works where ammonia annealing was used to implement graphitic nitrogen groups in activated phenolic resins (novolac).<sup>[38,39]</sup>

To further analyze the carbon structure, we applied Raman spectroscopy (Figure 4B). The positions as well as the full-width at half-maximum (FWHM) of the D- and G-mode and the  $I_D/I_G$ -ratios are listed in Table 4. The G-mode of all three samples is at

**Table 4.** Peak characteristics of the D- and G-mode of the Raman spectra.

Sample		Position [cm <sup>-1</sup> ]	FWHM [cm <sup>-1</sup> ]	$I_D/I_G$
$G^A\text{-C-Ar}$	D-mode	1316	155	1.67
	G-mode	1593	76	
$G^A\text{-C-CO}_2$	D-mode	1324	135	1.53
	G-mode	1600	70	
$G^A\text{-C-NH}_3$	D-mode	1326	126	1.89
	G-mode	1605	61	

1593–1605 cm<sup>-1</sup>, and the  $I_D/I_G$ -ratio ranges from 1.53 to 1.89, indicative of nanocrystalline graphitic carbon.<sup>[52,53]</sup> The sample  $G^A\text{-C-Ar}$  shows broader peaks (FWHM<sub>D</sub>:  $155 \text{ cm}^{-1}$  and FWHM<sub>G</sub>:  $76 \text{ cm}^{-1}$ ) due to a higher amount of amorphous carbon in the structure, which is in good agreement with TEM images seen in Figure 2.<sup>[54]</sup> The samples  $G^A\text{-C-CO}_2$  and  $G^A\text{-C-NH}_3$  show narrower peaks because the activation with carbon dioxide (FWHM<sub>D</sub>:  $135 \text{ cm}^{-1}$  and FWHM<sub>G</sub>:  $70 \text{ cm}^{-1}$ ) and ammonia (FWHM<sub>D</sub>:  $124 \text{ cm}^{-1}$  and FWHM<sub>G</sub>:  $61 \text{ cm}^{-1}$ ) prefers the removal of amorphous and less ordered carbon.<sup>[6,39]</sup>

The incompletely graphitic structure of the gyroidal carbons was confirmed with XRD (Figure 4C). Only the X-ray reflections

**Table 2.** Elemental composition of chemical analysis and the TGA measurements of the carbon samples and the carbon/sulfur hybrids (n.d.: not detected).

Sample	CHNOS analysis			TGA		
	C [mass%]	H [mass%]	N [mass%]	S [mass%]	O [mass%]	S [mass%]
$G^A\text{-C-Ar}$	$93.5 \pm 0.3$	$1.4 \pm 0.9$	$0.5 \pm 0.1$	n.d.	$4.6 \pm 0.2$	–
$G^A\text{-C-CO}_2$	$94.3 \pm 0.8$	$1.1 \pm 0.1$	$0.3 \pm 0.1$	n.d.	$4.3 \pm 1.0$	–
$G^A\text{-C-NH}_3$	$82.5 \pm 0.1$	$1.8 \pm 0.1$	$6.5 \pm 0.1$	n.d.	$9.2 \pm 0.1$	–
$G^A\text{-C-Ar/S}$	$29.0 \pm 0.3$	$0.5 \pm 0.1$	$0.2 \pm 0.1$	$67.3 \pm 0.8$	$3.0 \pm 0.5$	$68.1$
$G^A\text{-C-CO}_2/S$	$29.1 \pm 0.5$	$0.5 \pm 0.3$	$0.2 \pm 0.1$	$67.6 \pm 0.5$	$2.7 \pm 0.7$	$67.1$
$G^A\text{-C-NH}_3/S$	$25.8 \pm 0.3$	$0.4 \pm 0.1$	$2.0 \pm 0.1$	$67.8 \pm 0.6$	$4.1 \pm 0.9$	$67.5$

**Table 3.** Chemical composition of the NC-carbon samples measured with XPS (normalized to 100%) and bonding content of the N 1s peak (n.d.: not detectable).

Sample	C [mass%]	N [mass%]	O [mass%]	N1 at 398 eV [%]	N2 at 400 eV [%]	N–O at 404 eV [%]
$G^A\text{-C-Ar}$	93.3	n.d.	6.7	n.d.	n.d.	n.d.
$G^A\text{-C-CO}_2$	82.3	n.d.	17.7	n.d.	n.d.	n.d.
$G^A\text{-C-NH}_3$	86.0	5.0	9.0	21.6	60.3	18.1

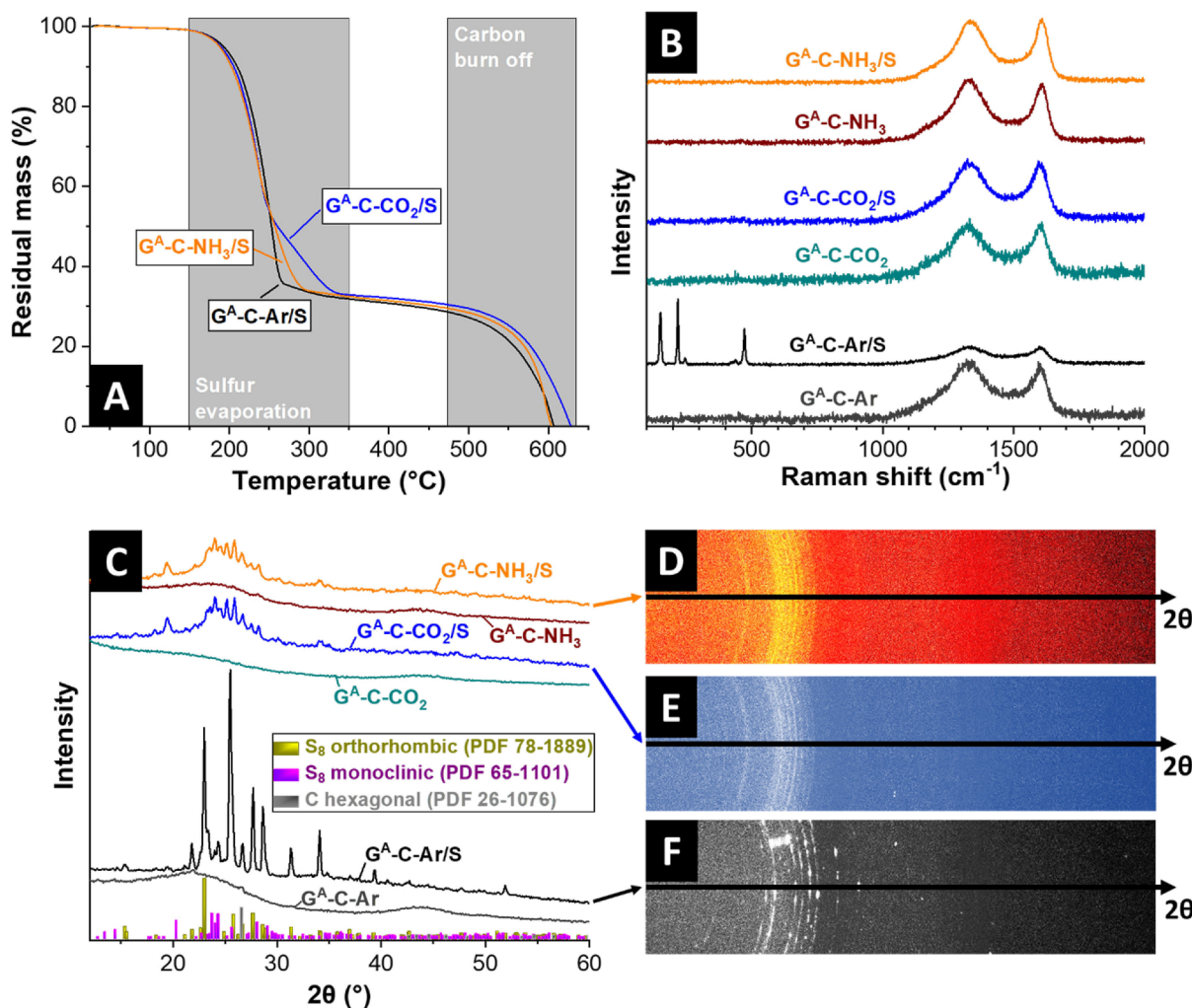


**Figure 4.** (A) Thermogravimetric analysis of the carbon/sulfur hybrids measured in synthetic air, (B) Raman spectra, and (C) XRD pattern of the carbon and the carbon/sulfur samples including the 2D XRD pattern (D–F).

of the (002) plane at  $23^\circ 2\theta$ , and (110) plane at  $44^\circ 2\theta$  of carbon can be observed for all samples.<sup>[53,55]</sup> The reflections of G<sup>A</sup>-C-Ar are more intense than for the other two samples, even though the Raman spectra showed that all three materials have a similar carbon structure. This can be explained by the higher porosity of the CO<sub>2</sub> and NH<sub>3</sub> activated samples, which reduces the stacking of graphene layers and the overall signal strength.<sup>[53]</sup>

## 2.2. Characterization of the Carbon/Sulfur Hybrids

We choose melt infiltration to prepare the carbon/sulfur hybrid electrodes based on our previous experience with microporous carbons.<sup>[6]</sup> The TGA data in Figure 4A confirm an average sulfur content of 66.6 mass% by the mass loss due to the evaporation of the sulfur in the range from 200°C to 350°C. This sulfur loading was corroborated by the chemical analysis where the samples showed values of 67.3–67.8 mass% (Table 3). Based on these values, the amount of electrolyte was calculated, and the performance of the LiS-battery was normalized to the sulfur

mass. The TGA data also give insights into the nanoconfinement of sulfur. The curve of G<sup>A</sup>-C-Ar/S exhibits only one single step for the sulfur evaporation, while G<sup>A</sup>-C-CO<sub>2</sub>/S and G<sup>A</sup>-C-NH<sub>3</sub>/S data have a lower slope at higher temperatures ( $\sim 275^\circ\text{C}$ ). Sulfur confined in micropores evaporates at higher temperatures compared to bulk sulfur.<sup>[15]</sup> Since TGA measurements were carried out in synthetic air, the carbon burn-off is identical from 500°C. Note that all samples achieve finally complete volatilization (i.e., 100% mass loss), which confirms the absence of incombustible (inorganic) impurities in the samples.

The position and FWHM of the carbon-related D- and G-modes were not affected after sulfur infiltration since the temperature of 155°C is too low to change the carbon structure (Figure 4B). The lower intensity of the carbon signal in G<sup>A</sup>-C-Ar/S results from the high signal strength of crystalline sulfur below 500 cm<sup>-1</sup>. The other two hierarchically porous samples have no observable sulfur signals, which indicates homogeneously confined sulfur inside the pores. The crystalline nature of sulfur was further investigated by XRD (Figure 4C–F). In all three carbon/sulfur samples, typical crystalline sulfur diffractions are obvious. While the sample G<sup>A</sup>-C-Ar/S showed

the presence of orthorhombic and monoclinic sulfur, the sulfur inside G<sup>A</sup>-C-CO<sub>2</sub>/S and G<sup>A</sup>-C-NH<sub>3</sub>/S is only monoclinic. Sulfur forms first a monoclinic phase when it solidifies which converts to an orthorhombic stricter later. The mesoporous confinement of the carbon hinders the formation of such an orthorhombic crystal structure, as it is the case for G<sup>A</sup>-C-Ar/S where sulfur is additionally located outside the mesopores. The sample G<sup>A</sup>-C-Ar/S has also sulfur which is not confined to the mesopores which can faster convert to orthorhombic sulfur. Using the Scherrer equation, it is possible to estimate the average domain size of the sulfur crystals.<sup>[56]</sup> The orthorhombic sulfur in the sample G<sup>A</sup>-C-Ar/S shows no peak broadening beyond from finite domain sizes; therefore, these crystals must be larger than 100–200 nm and cannot completely fit into the gyroidal structure. The presence of large sulfur crystals is confirmed from the spotted Debye rings seen in the 2D diffraction pattern (Figure 4F). The average domain size of the sulfur in G<sup>A</sup>-C-CO<sub>2</sub>/S and G<sup>A</sup>-C-NH<sub>3</sub>/S is approximately 60 nm, which is larger than the pore diameter of around 20 nm. Therefore, sulfur crystals are predominating growing among the mesopores. Besides the sulfur peaks from G<sup>A</sup>-C-CO<sub>2</sub>/S and G<sup>A</sup>-C-NH<sub>3</sub>/S, we observed also a broad amorphous peak, which can only partly be related to non-graphitic carbon. These large reflections occur due to sulfur within the micropores, unable to grow to large crystals due to the confinement.<sup>[6]</sup> By having a look at the 2D diffraction pattern of G<sup>A</sup>-C-CO<sub>2</sub>/S and G<sup>A</sup>-C-NH<sub>3</sub>/S, we see complete Debye rings of the sulfur phase, which indicates a very homogeneous distribution of the sulfur in the carbon pores.

The distribution of the elements was visualized by a TEM-EDX mapping (Figure 5). G<sup>A</sup>-C-Ar/S shows an overlapping of the

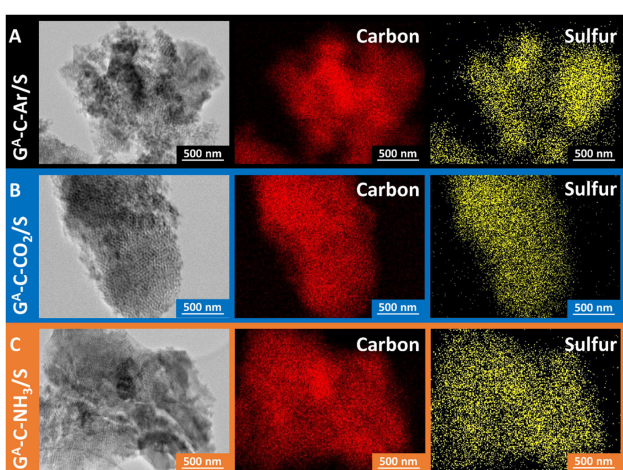


**Figure 5.** TEM images of the samples (A) G<sup>A</sup>-C-Ar/S, (B) G<sup>A</sup>-C-CO<sub>2</sub>/S, and (C) G<sup>A</sup>-C-NH<sub>3</sub>/S including EDX mapping of carbon and sulfur.

carbon and sulfur mapping in the entire analyzed area, but the intensity of carbon and sulfur is different at certain locations (Figure 5). This inhomogeneous intensity distribution indicates that the sulfur is not filling the pores completely and is also found on the external surface in large amounts. External sulfur aligns also with the large sulfur domain sizes calculated from

XRD. The samples G<sup>A</sup>-C-CO<sub>2</sub>/S and G<sup>A</sup>-C-NH<sub>3</sub>/S show a very homogeneous carbon and sulfur distribution, supporting the XRD data and the conclusion of sulfur confinement within the pores.

### 2.3. Electrochemical Characterization

The carbon/sulfur hybrids were tested as LiS-battery cathodes at low C-rates (0.1C discharge, 0.2C charge). The discharge capacity and the Coulombic efficiency of these measurements with the voltage profile of selected cycles are plotted in Figure 6. Initially, G<sup>A</sup>-C-Ar/S shows a high capacity of more than 700 mAh/g<sub>sulfur</sub> for the first few cycles, followed by a rapid decrease, and reaching 151 mAh/g<sub>sulfur</sub> after 100 cycles. Since sulfur was incompletely filling the micro- and mesopores, it is likely that polysulfides are easily dissolved in the electrolyte, which results in stronger sulfur shuttling. It is also likely that the electron transfer from the carbon towards the sulfur is hindered, due to the low accessible surface area. We also see distinct features in the measured voltage profile shown in Figure 6B. Usually, two plateaus are expected for LiS-batteries during discharge in the range of 2.3–2.4 V and at ~2.1 V vs. Li/Li<sup>+</sup> (as was seen for G<sup>A</sup>-C-CO<sub>2</sub>/S, Figure 6C). The first plateau at 2.3–2.4 V occurs from the reduction of elemental sulfur to large Li-polysulfides (Li<sub>2</sub>S<sub>4–8</sub>).<sup>[57,58]</sup> The second plateau is related to the further reduction to small Li-polysulfides (Li<sub>2</sub>S<sub>2</sub> and Li<sub>2</sub>S).<sup>[57,58]</sup> The voltage profile of the sample G<sup>A</sup>-C-Ar/S shows a first plateau in the range of 2.2–2.3 V vs. Li/Li<sup>+</sup>, then a decrease to almost 1.8 V vs. Li/Li<sup>+</sup> which indicates the formation of small polysulfides, followed by a potential increase. During the discharge of the cell, the potential is increasing again and reaches around 2.1 V vs. Li/Li<sup>+</sup>, which is characteristic for the reaction of larger polysulfides. Sulfur, which is not confined to the carbon pores, is expected to react completely before the sulfur within the pores becomes accessible. This is well visible for G<sup>A</sup>-C-Ar/S, where the sulfur is not homogeneously distributed because the mesopores cannot accommodate the large sulfur content. This finding is supported by XRD result, where the orthorhombic structure indicates the formation of much larger crystals, which do not fit inside the pores. From a practical application point of view, however, such high sulfur mass loadings are desirable.<sup>[2]</sup> Sulfur inside the porous carbon is most probably only accessible for the electrolyte when the sulfur on the outside of the particles has been dissolved. The larger polysulfides then increase the potential in the voltage profile by reacting to smaller units. This behavior is reduced when the LiS cell is running for a larger number of cycles because more pathways are generated, and a lower capacity is obtained due to polysulfide shuttling.

The G<sup>A</sup>-C-CO<sub>2</sub>/S samples show typical LiS-battery voltage profiles with the two plateaus for the reduction of sulfur towards Li<sub>2</sub>S for all cycles (Figure 6). The initial specific capacity of 1098 mAh/g<sub>sulfur</sub> remains above 800 mAh/g<sub>sulfur</sub> after 50 cycles and above 700 mAh/g<sub>sulfur</sub> after 100 cycles measured with a C-rate of 0.1C for the discharging and 0.2C for the charging step.

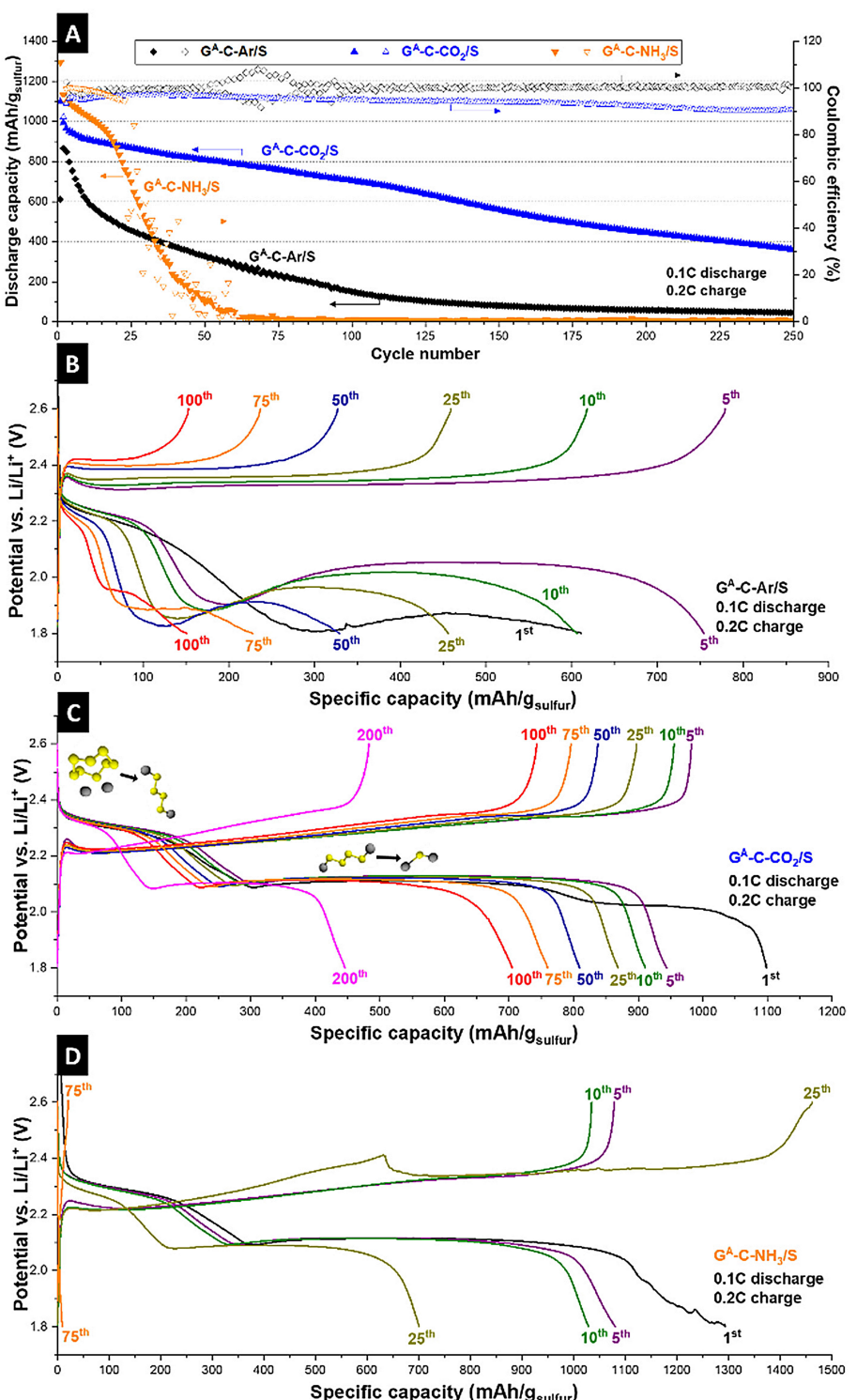


**Figure 6.** (A) Electrochemical performance of the LiS-batteries at low C-rates (0.1C discharge and 0.2C charge) and (B–D) corresponding voltage profiles of selected cycles.

After 100 cycles, the capacity fade increases and a specific capacity of about 450 mAh/g<sub>sulfur</sub> is reached after 200 cycles.

G<sup>A</sup>-C-NH<sub>3</sub>/S shows among all samples the highest initial specific capacity of about 1300 mAh/g<sub>sulfur</sub>, corresponding to 78% of the theoretical specific capacity (Figure 6D). After 10 cycles, the capacity is still above 1000 mAh/g<sub>sulfur</sub> which is

higher than the capacity for G<sup>A</sup>-C-CO<sub>2</sub>/S. After the 20<sup>th</sup> cycle, capacity and Coulombic efficiency decreases significantly. The voltage profile for the 25<sup>th</sup> charging cycle in Figure 6D shows a large plateau at 2.3–2.4 V vs. Li/Li<sup>+</sup>. This region shows a large energy consumption and we assume the decomposition of nitrogen groups.

The discharge specific capacity after 50 cycles is 100 mAh/g<sub>sulfur</sub> and only ~10 mAh/g<sub>sulfur</sub> after 75 cycles. Seemingly, nitrogen groups enable a higher specific capacity initially because of the affinity of sulfur towards the carbon surface in good agreement with previous works.<sup>[23,25,26,61]</sup> Yet, this performance cannot be maintained for a large number of cycles. It is likely that degradation of nitrogen- and oxygen-containing functional groups (mainly pyrrolic, amine, and amide groups) causes the poor long-time electrochemical performance. Other studies which propose that nitrogen groups enhance the electrochemical performance of LiS-batteries often have graphitic or pyridinic nitrogen and only low amount of amorphous carbon in contrast to our mainly non-graphitic carbon host.<sup>[23,25,62-64]</sup> These features might be crucial for nitrogen-doped carbon materials for LiS-batteries.

To have better understanding on the performance stability, we carried out post-mortem XPS, TEM, and EDX mapping measurements of the cathode after the long-time stability test at low C-rates. The XPS spectra (Supporting Information, Figure S4) show that a solid electrolyte interphase (SEI) was formed. The binding energies of the C1s, N1s, F1s, Li1s, and O1s in Figure S4 fit the energies found in the literature for SEI components like LiTFSI, Li<sub>2</sub>CO<sub>3</sub>, or polysulfides.<sup>[59,60]</sup> The TEM images (Figure S5) show that the gyroidal structure was maintained after the electrochemical measurements. A TEM-EDX mapping was conducted (Figure S6), which shows that carbon, sulfur, nitrogen, and oxygen remain well distributed in the sample. The measured nitrogen is not only related to nitrogen functional groups but also to the SEI which contains decomposed products of the electrolyte.

An overview of the LiS-performance data normalized to the mass of sulfur and the whole electrode mass with values from the literature is given in Table 5. We choose only carbon/sulfur

materials which were produced with similar synthesis conditions (melt infiltration) and measured under comparable conditions (e.g., same electrolyte and similar potential window). Other sulfur infiltration methods like the in-situ formation from Na<sub>2</sub>S<sub>2</sub>O<sub>3</sub> also show high specific capacities of >1300 mAh/g<sub>sulfur</sub> for the first cycle with a quite stable performance.<sup>[65]</sup> The carbon host can only be compared when the same infiltration method is used because it has a significant influence on the performance.<sup>[6,66]</sup> Another approach to producing stable LiS-batteries can be achieved by C/Li<sub>2</sub>S-hybrids instead C/S-hybrids.<sup>[67]</sup> Such system can reach a specific capacity of >1100 mAh/g<sub>sulfur</sub> (~800 mAh/g<sub>sulfur</sub> after 100 cycles with a sulfur loading of ~61 mass%).<sup>[67]</sup> The comparison of different C/S-hybrid cathode materials measured at similar conditions in Table 5 shows improved performance for the activated gyroidal carbons. The gyroidal carbon materials used by Werner et al. show higher stability normalized to the amount of sulfur (810 mAh/g<sub>sulfur</sub> after 100 cycles), but this study used a low carbon to sulfur ratio of only 1:1.<sup>[2,17]</sup> Even though the sulfur content was relatively low, a relatively high specific capacity normalized to the electrode of 365 mAh/g<sub>electrode</sub> after 100 cycles was reported,<sup>[17]</sup> which is lower compared to G<sup>A</sup>-C-CO<sub>2</sub>/S after 100 cycles (387 mAh/g). The high electrode normalized specific capacity of Werner et al. was reached because they were not using additional conductive additives for the low C-rate measurements even though the sulfur content was relatively low.<sup>[17]</sup> Nevertheless, conductive additives are necessary to reach high C-rates and to enhance the overall performance.<sup>[68]</sup> The gyroidal-templated carbon material from Choudhury et al. has a relatively low electrode normalized specific capacity of 236 mAh/g<sub>electrode</sub> after 100 cycles.<sup>[18]</sup> Other comparable micro-porous and mesoporous materials from the literature show after 100 cycles a lower specific capacity than the G<sup>A</sup>-C-CO<sub>2</sub>/S

**Table 5.** Specific discharge capacity of all three hybrid electrodes after 1, 5, and 100 cycles at low discharge/charge rates with a comparison of other carbon materials for LiS-batteries from the literature.<sup>[a]</sup>

Electrode material	Porosity type	SSA <sub>BET</sub> [m <sup>2</sup> /g]	Potential vs. Li/Li <sup>+</sup> [V]	Specific capacity [mAh/g] <sup>[b]</sup>				100 <sup>th</sup> cycle per sulfur	Ref.	
				1 <sup>st</sup> cycle per sulfur	5 <sup>th</sup> cycle per electrode	per sulfur	per electrode			
G <sup>A</sup> -C-Ar/S	mesoporous	197	1.8–2.6	611	336	754	414	151	this work	
G <sup>A</sup> -C-CO <sub>2</sub> /S	micro- & mesoporous	1264	1.8–2.6	1098	603	944	519	704	this work	
G <sup>A</sup> -C-NH <sub>3</sub> /S	micro- & mesoporous	1191	1.8–2.6	1294	711	1080	593	9	5	this work
G <sup>A</sup> MC-15-900 °C	mesoporous	600	1.5–2.8	1392	626	1070	482	728	[17]	
aG <sup>D</sup> MC-15-CO <sub>2</sub> -10 h	micro- & mesoporous	2030	1.5–2.8	1700	765	1130	509	810	[17]	
Gyroid-templated-C	micro- & mesoporous	885	1.8–2.6	580	319	590	324	430	236	[18]
PNC-S-annealed	microporous	529	1.8–2.6	1063	601	661	374	560	317	[6]
PNC <sub>act</sub> -S-annealed	microporous	2700	1.8–2.6	1159	656	662	375	604	342	[6]
OLC-S-1	mesoporous	400	1.8–2.6	950	530	730	407	670	374	[66]
Carbon aerogel	micro- & mesoporous	1395	1.8–2.8	910	364	800	320	600	240	[71]
BCP templated carbon	micro- & mesoporous	630	1.8–2.6	1050	568	800	433	530	287	[72]
Kroll-C/S_53	micro- & mesoporous	1990	1.8–2.6	1089	577	~1000	530	817 (80 <sup>th</sup> cycle)	433 (80 <sup>th</sup> cycle)	[9]

[a] The specific capacity is normalized to the mass of sulfur and to the mass of the whole electrode. [b] Discharge: 0.1C; charge: 0.2C

material; the latter had a capacity of 704 mAh/g<sub>sulfur</sub> which corresponds to 387 mAh/g<sub>electrode</sub> (cycled at 0.1C for discharging and 0.2C for charging).

The performance of the gyroidal carbon materials was also investigated at higher charge and discharge rates (Figure 7).

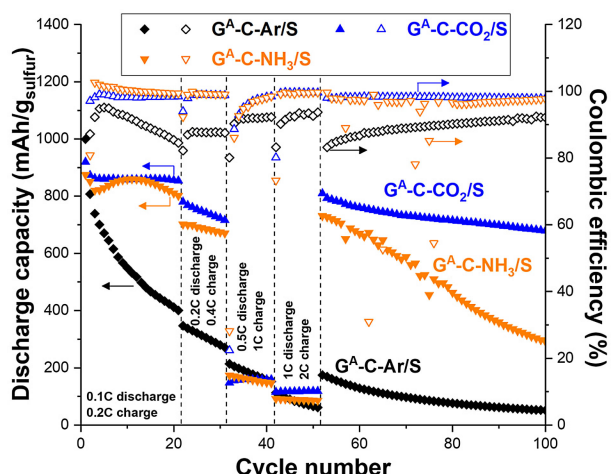


Figure 7. Electrochemical performance of G<sup>A</sup>-C-Ar/S, G<sup>A</sup>-C-CO<sub>2</sub>/S, and G<sup>A</sup>-C-NH<sub>3</sub>/S at different rates.

The sample G<sup>A</sup>-C-Ar/S does provide stable performance, yet only a small effect of scan rates is seen for the specific capacity. The specific capacity of G<sup>A</sup>-C-NH<sub>3</sub>/S and G<sup>A</sup>-C-CO<sub>2</sub>/S slightly reduces at 0.2C (discharge) and 0.4C (charge), but there is a large performance drop below 200 mAh/g<sub>sulfur</sub> at higher C-rates. It is likely that the crystalline sulfur within the mesopores hinders the intrapore mass transport. At low rates, this issue is not a limiting factor because the system is given sufficient time for sulfide dissolution. At high rates, the sulfur in the mesopores cannot be fully capitalized on; therefore, activated and non-activated materials show a similar performance. By reducing the C-rate again to the initial charge/discharge rate, the high specific capacity with a stable performance is restored, especially for G<sup>A</sup>-C-CO<sub>2</sub>/S.

Electrochemical impedance spectroscopy of the initial cells at 2.6 V vs. Li/Li<sup>+</sup> was carried out, and the Nyquist plot is shown in the Supporting Information, Figure S3. The Ohmic resistance ( $R_0$ ) is influenced by the electrolyte resistance, the current collector, and the cell design and all material showed a very similar value for  $R_0$ .<sup>[69,70]</sup> This relates to the use of the same setup and cell design for all measurements. The charge transfer resistance ( $R_{ct}$ ) in the medium-to-high-frequency range correlates to the electrochemical kinetics and is also similar for all three hybrid cathode materials.<sup>[69,70]</sup> The  $R_{ct}$  for G<sup>A</sup>-C-CO<sub>2</sub>/S is slightly smaller compared to the value of G<sup>A</sup>-C-Ar/S and G<sup>A</sup>-C-NH<sub>3</sub>/S which is in line with the similar performance at high C-rates (1C discharge and 2C charge), where G<sup>A</sup>-C-CO<sub>2</sub>/S also performs better.

### 3. Conclusions

In this study, we prepared ordered porous carbons by co-assembly of a commercial resol with an ISO block copolymer. The latter was pyrolyzed and in-situ activated in different atmospheres, namely Ar, CO<sub>2</sub>, or NH<sub>3</sub>. All samples had micro- and mesopores, with the smallest volume of micropores and smallest total pore volume after treatment just in argon (G<sup>A</sup>-C-Ar; non-activated sample). Larger pore volumes were obtained after activation with CO<sub>2</sub> (G<sup>A</sup>-C-CO<sub>2</sub>) or NH<sub>3</sub> (G<sup>A</sup>-C-NH<sub>3</sub>). We hybridized all samples with sulfur using melt infiltration to test the resulting materials as cathodes for LiS-batteries. The pore structure of the non-activated sample was not suitable to achieve a homogeneous phase distribution. The ammonia activation increased microporosity and formed nitrogen functionalities, identified by XPS as pyridinic, pyrrolic, amine, and amide groups. These groups lead to a superior initial capacity (~1300 mAh/g<sub>sulfur</sub> in the 1<sup>st</sup> cycle), but simultaneously drastically reducing the long-term stability. The activation with CO<sub>2</sub> did not change the chemical composition much compared to the non-activated argon sample but enhanced the total pore volume and the microporosity. Thereby, it was possible to obtain a homogeneous carbon/sulfur hybrid by melt infiltration. This cathode material showed a slightly lower initial capacity of 1100 mAh/g<sub>sulfur</sub> but rather stable performance with a specific capacity of more than 700 mAh/g<sub>sulfur</sub> after 100 cycles. While NH<sub>3</sub> treatment did introduce nitrogen to our samples, it failed to generate graphitic nitrogen. Thereby, we see a severe drop in performance and poor cycling stability of the sample G<sup>A</sup>-C-NH<sub>3</sub>. Obviously, the pore structure is of high importance for the performance of LiS-batteries. We also see that nitrogen-doping may enhance the initial capacity, but there may be a poor performance stability depending on the type of nitrogen.

### Acknowledgements

This project was supported by the INM FOCUS project funding (POLION). J.S. and J.J. acknowledge support by the Center for Materials Research at JLW Gießen. The authors kindly acknowledge the continuing support of Eduard Arzt (INM). We thank Ralph Schäfer from Allnex Germany GmbH for the supply of Phenodur, Andrea Jung (INM) for the CHNS and O analysis, and Peng Zhang (INM) for the SAXS measurements. We also acknowledge the help from Ingrid Grobelsek (INM) regarding the XRD analysis, we thank Nicolas Jäckel (INM) for discussions, and we are grateful to Lars Borchardt (TU Dresden) for support and discussions.

### Conflict of Interest

The authors declare no conflict of interest.

**Keywords:** activation • carbon • energy storage • lithium-sulfur battery • self-assembly

- [1] M. Wild, L. O'Neill, T. Zhang, R. Purkayastha, G. Minton, M. Marinescu, G. Offer, *Energy Environ. Sci.* **2015**, *8*, 3477–3494.
- [2] L. Borchardt, M. Oschatz, S. Kaskel, *Chem. – Eur. J.* **2016**, *22*, 7324–7351.
- [3] S. Pelletier, O. Jabali, G. Laporte, M. Veneroni, *Trans. Res. Part B: Method.* **2017**, *103*, 158–187.
- [4] L. Medenbach, P. Adelhelm, *Top. Curr. Chem.* **2017**, *375*, 81.
- [5] Z. Li, X. Li, Y. Liao, X. Li, W. Li, *J. Power Sources* **2016**, *334*, 23–30.
- [6] S. Choudhury, B. Krüner, P. Massuti-Ballester, A. Tolosa, C. Prehal, I. Grobelsek, O. Paris, L. Borchardt, V. Presser, *J. Power Sources* **2017**, *357*, 198–208.
- [7] X. Ji, K. T. Lee, L. F. Nazar, *Nat. Mater.* **2009**, *8*, 500–506.
- [8] J. Song, T. Xu, M. L. Gordin, P. Zhu, D. Lv, Y. B. Jiang, Y. Chen, Y. Duan, D. Wang, *Adv. Funct. Mater.* **2014**, *24*, 1243–1250.
- [9] M. Oschatz, S. Thieme, L. Borchardt, M. R. Lohe, T. Biemelt, J. Brückner, H. Althues, S. Kaskel, *Chem. Commun.* **2013**, *49*, 5832–5834.
- [10] A. Schneider, C. Suchomski, H. Sommer, J. Janek, T. Brezesinski, *J. Mater. Chem. A* **2015**, *3*, 20482–20486.
- [11] G. Xu, B. Ding, P. Nie, L. Shen, H. Dou, X. Zhang, *ACS Appl. Mater. Interfaces* **2013**, *6*, 194–199.
- [12] J.-J. Kim, H. S. Kim, J. Ahn, K. J. Lee, W. C. Yoo, Y.-E. Sung, *J. Power Sources* **2016**, *306*, 617–622.
- [13] C. Reitz, B. Breitung, A. Schneider, D. Wang, M. von der Lehr, T. Leichtweiss, J. r. Janek, H. Hahn, T. Brezesinski, *ACS Appl. Mater. Interfaces* **2016**, *8*, 10274–10282.
- [14] T. Wang, K. Kretschmer, S. Choi, H. Pang, H. Xue, G. Wang, *Small Methods* **2017**, *1*, 1700089.
- [15] C. Fu, B. M. Wong, K. N. Bozhilov, J. Guo, *Chem. Sci.* **2016**, *7*, 1224–1232.
- [16] A. Schneider, J. Janek, T. Brezesinski, *Phys. Chem. Chem. Phys.* **2017**, *19*, 8349–8355.
- [17] J. r. G. Werner, S. S. Johnson, V. Vijay, U. Wiesner, *Chem. Mater.* **2015**, *27*, 3349–3357.
- [18] S. Choudhury, M. Agrawal, P. Formanek, D. Jehnichen, D. Fischer, B. Krause, V. Albrecht, M. Stamm, L. Ionov, *ACS Nano* **2015**, *9*, 6147–6157.
- [19] J. r. G. Werner, T. N. Hoheisel, U. Wiesner, *ACS Nano* **2013**, *8*, 731–743.
- [20] J. Song, M. L. Gordin, T. Xu, S. Chen, Z. Yu, H. Sohn, J. Lu, Y. Ren, Y. Duan, D. Wang, *Angew. Chem. Int. Ed.* **2015**, *54*, 4325–4329.
- [21] C. Wang, K. Su, W. Wan, H. Guo, H. Zhou, J. Chen, X. Zhang, Y. Huang, *J. Mater. Chem. A* **2014**, *2*, 5018–5023.
- [22] F. Sun, J. Wang, H. Chen, W. Li, W. Qiao, D. Long, L. Ling, *ACS Appl. Mater. Interfaces* **2013**, *5*, 5630–5638.
- [23] S. Niu, G. Zhou, W. Lv, H. Shi, C. Luo, Y. He, B. Li, Q.-H. Yang, F. Kang, *Carbon* **2016**, *109*, 1–6.
- [24] F. Hippauf, W. Nickel, G. P. Hao, K. Schwedtmann, L. Giebel, S. Oswald, L. Borchardt, S. Doerfler, J. J. Weigand, S. Kaskel, *Adv. Mater. Interfaces* **2016**, *3*, 1600508.
- [25] X. G. Sun, X. Wang, R. T. Mayes, S. Dai, *ChemSusChem* **2012**, *5*, 2079–2085.
- [26] X. Wang, Z. Zhang, Y. Qu, Y. Lai, J. Li, *J. Power Sources* **2014**, *256*, 361–368.
- [27] W. Shen, W. Fan, *J. Mater. Chem. A* **2013**, *1*, 999–1013.
- [28] Z. Liu, K. Xiao, H. Guo, X. Ning, A. Hu, Q. Tang, B. Fan, Y. Zhu, X. Chen, *Carbon* **2017**, *117*, 163–173.
- [29] N. A. Travlou, T. J. Bandosz, *Carbon* **2017**, *117*, 228–239.
- [30] Y. Wu, S. Fang, Y. Jiang, *J. Mater. Chem.* **1998**, *8*, 2223–2227.
- [31] Z. Wang, L. Sun, F. Xu, X. Peng, Y. Zou, H. Chu, L. Ouyang, M. Zhu, *RSC Adv.* **2016**, *6*, 1422–1427.
- [32] L.-F. Chen, X.-D. Zhang, H.-W. Liang, M. Kong, Q.-F. Guan, P. Chen, Z.-Y. Wu, S.-H. Yu, *ACS Nano* **2012**, *6*, 7092–7102.
- [33] X. Liu, Y. Zhou, W. Zhou, L. Li, S. Huang, S. Chen, *Nanoscale* **2015**, *7*, 6136–6142.
- [34] C. L. Mangun, K. R. Benak, J. Economy, K. L. Foster, *Carbon* **2001**, *39*, 1809–1820.
- [35] B. Stöhr, H. Boehm, R. Schlägl, *Carbon* **1991**, *29*, 707–720.
- [36] J. S. Noh, J. A. Schwarz, *Carbon* **1990**, *28*, 675–682.
- [37] M. Widmaier, B. Krüner, N. Jäckel, M. Aslan, S. Fleischmann, C. Engel, V. Presser, *J. Electrochem. Soc.* **2016**, *163*, A2956–A2964.
- [38] X. Wang, C.-G. Liu, D. Neff, P. F. Fulvio, R. T. Mayes, A. Zhamu, Q. Fang, G. Chen, H. M. Meyer, B. Z. Jang, *J. Mater. Chem. A* **2013**, *1*, 7920–7926.
- [39] B. Krüner, A. Schreiber, A. Tolosa, A. Quade, F. Badaczewski, T. Pfaff, B. M. Smarsly, V. Presser, *Carbon* **2018**, *132*, 220–231.
- [40] M. A. Hillmyer, F. S. Bates, *Macromolecules* **1996**, *29*, 6994–7002.
- [41] J. Chatterjee, S. Jain, F. S. Bates, *Macromolecules* **2007**, *40*, 2882–2896.
- [42] V. Presser, J. McDonough, S.-H. Yeon, Y. Gogotsi, *Energy Environ. Sci.* **2011**, *4*, 3059–3066.
- [43] A. Vishnyakov, P. I. Ravikovitch, A. V. Neimark, *Langmuir* **1999**, *15*, 8736–8742.
- [44] G. Y. Gor, M. Thommes, K. A. Cychosz, A. V. Neimark, *Carbon* **2012**, *50*, 1583–1590.
- [45] S. Brunauer, P. H. Emmett, E. Teller, *J. Amer. Chem. Soc.* **1938**, *60*, 309–319.
- [46] S. S. Zhang, *Energies* **2012**, *5*, 5190–5197.
- [47] T. H. Epps, E. W. Cochran, C. M. Hardy, T. S. Bailey, R. S. Waletzko, F. S. Bates, *Macromolecules* **2004**, *37*, 7085–7088.
- [48] M. Thommes, K. Kaneko, A. V. Neimark, J. P. Olivier, F. Rodriguez-Reinoso, J. Rouquerol, K. S. Sing, *Pure Appl. Chem.* **2015**, *87*, 1051–1069.
- [49] J.-P. Boudou, P. Parent, F. Suarez-Garcia, S. Villar-Rodil, A. Martínez-Alonso, J. Tascón, *Carbon* **2006**, *44*, 2452–2462.
- [50] R. Arrigo, M. Hävecker, R. Schlägl, D. S. Su, *Chem. Commun.* **2008**, 4891–4893.
- [51] Y. Zhao, X. Liu, Y. Han, *RSC Adv.* **2015**, *5*, 30310–30330.
- [52] A. C. Ferrari, J. Robertson, *Phys. Rev. B* **2000**, *61*, 14095.
- [53] K. Faber, F. Badaczewski, M. Oschatz, G. Mondin, W. Nickel, S. Kaskel, B. M. Smarsly, *J. Phys. Chem. C* **2014**, *118*, 15705–15715.
- [54] P. K. Chu, L. Li, *Mater. Chem. Phys.* **2006**, *96*, 253–277.
- [55] P. Debye, P. Scherrer, *Nachrichten von der Gesellschaft der Wissenschaften zu Göttingen, Mathematisch-Physikalische Klasse* **1917**, *1917*, 180–188.
- [56] P. Scherrer, *Nachrichten von der Gesellschaft der Wissenschaften zu Göttingen* **1918**, *2*, 98–100.
- [57] J. Kulisch, H. Sommer, T. Brezesinski, J. Janek, *Phys. Chem. Chem. Phys.* **2014**, *16*, 18765–18771.
- [58] N. Jayaprakash, J. Shen, S. S. Moganty, A. Corona, L. A. Archer, *Angew. Chem.* **2011**, *123*, 6026–6030.
- [59] E. Markevich, G. Salitra, A. Rosenman, Y. Talyosef, F. Chesneau, D. Aurbach, *J. Mater. Chem. A* **2015**, *3*, 19873–19883.
- [60] H. Metelmann, *Justus-Liebig-Universität Gießen*, **2017**.
- [61] Y. Qiu, W. Li, W. Zhao, G. Li, Y. Hou, M. Liu, L. Zhou, F. Ye, H. Li, Z. Wei, *Nano Lett.* **2014**, *14*, 4821–4827.
- [62] L. Chen, Y. Liu, M. Ashuri, C. Liu, L. L. Shaw, *J. Mater. Chem. A* **2014**, *2*, 18026–18032.
- [63] Q. Li, Z. Zhang, Z. Guo, Y. Lai, K. Zhang, J. Li, *Carbon* **2014**, *78*, 1–9.
- [64] G. Zhou, Y. Zhao, A. Manthiram, *Adv. Energy Mater.* **2015**, *5*, 1402263.
- [65] B. Papandrea, X. Xu, Y. Xu, C.-Y. Chen, Z. Lin, G. Wang, Y. Luo, M. Liu, Y. Huang, L. Mai, X. Duan, *Nano Res.* **2016**, *9*, 240–248.
- [66] S. Choudhury, M. Zeiger, P. Massuti-Ballester, S. Fleischmann, P. Formanek, L. Borchardt, V. Presser, *Sustainable Energy & Fuels* **2017**, *1*, 84–94.
- [67] G. Tan, R. Xu, Z. Xing, Y. Yuan, J. Lu, J. Wen, C. Liu, L. Ma, C. Zhan, Q. Liu, T. Wu, Z. Jian, R. Shahbazian-Yassar, Y. Ren, D. J. Miller, L. A. Curtiss, X. Ji, K. Amine, *Nat. Energy* **2017**, *2*, 17090.
- [68] A. Jozwiuk, H. Sommer, J. Janek, T. Brezesinski, *J. Power Sources* **2015**, *296*, 454–461.
- [69] N. A. Cañas, K. Hirose, B. Pascucci, N. Wagner, K. A. Friedrich, R. Hiesgen, *Electrochim. Acta* **2013**, *97*, 42–51.
- [70] J. Zhang, Y. Shi, Y. Ding, L. Peng, W. Zhang, G. Yu, *Adv. Energy Mater.* **2017**, *7*, 1602876.
- [71] K. Balakumar, N. Kalaiselvi, *RSC Adv.* **2015**, *5*, 34008–34018.
- [72] S. Choudhury, D. Fischer, P. Formanek, M. Stamm, L. Ionov, *Adv. Mater. Interfaces* **2018**, *5*, 1701116.

Manuscript received: February 23, 2018  
Version of record online: April 26, 2018